communications physics

Article

https://doi.org/10.1038/s42005-024-01634-5

Experimental investigation of geometric quantum speed limits in an open quantum system

Check for updates

Diego Paiva Pires [1], Eduardo R. deAzevedo[2], Diogo O. Soares-Pinto [2], Frederico Brito [2,3] ✉ & Jefferson G. Filgueiras[2,4,5]

The quantum speed limit (QSL) is a fundamental lower bound on the evolution time for quantum systems, and its tightness has been observed to be dependent on the properties of the physical process. However, experimental studies exploring the QSL in open quantum systems are still missing. Here, we studied geometric quantum speed limits of a qubit subject to decoherence in an ensemble of chloroform molecules in a Nuclear Magnetic Resonance experiment. We controlled the system-reservoir interaction and the spin relaxation rates by adding a paramagnetic salt, allowing the observation of both Markovian and non-Markovian open system dynamics for the qubit. We used two distinguishability measures of quantum states to assess the speed of the qubit evolution: the quantum Fisher information (QFI) and Wigner-Yanase skew information (WY). For non-Markovianity and low salt concentrations, we found crossovers between QSLs related to those metrics. The WY metric sets the tighter QSL for high concentrations and Markovian dynamics. We also show that QSLs are sensitive even to small fluctuations in spin magnetization.

One of the core concepts of quantum mechanics is the uncertainty principle. While this relationship is well known for non-commuting observables, e.g., position and momentum, the time-energy uncertainty relation has been controversial over decades, resulting in several attempts to address this issue[1,2]. In their seminal work, Mandelstam and Tamm (MT)[3] reinterpreted this question by introducing the concept of quantum speed limit (QSL), which is a threshold imposed by quantum mechanics to the minimum evolution time between two orthogonal states. In this setting, Margolus and Levitin (ML)[4] derived a bound for the orthogonalization time of pure quantum states that scales with the inverse of the mean energy of the system.

Over a decade ago, Taddei et al.[5] have presented a general QSL bound based on the quantum Fisher information, valid for both unitary and nonunitary evolutions. At the same time, del Campo et al.[6] obtained a QSL relying on the relative purity, finding evidence that the spectral property of the noise would have an influence on the speed of evolution. In turn, Deffner and Lutz[7] introduced a QSL bound in terms of the operator norm of the generator of the nonunitary dynamics. Such an approach allowed them to investigate the influence of non-Markovianity on the evolution rate, finding that, for the Jaynes-Cummings model, its effect could lead to a faster evolution. QSLs have been addressed for either closed and open quantum systems[8–16], and find applications ranging from quantum many-body systems[17–23], to quantum thermodynamics[24–27]. In the context of nonequilibrium quantum dynamics, ref. 28 provides an extensive review on quantum speed limit bounds of several dynamical evolutions, particularly focusing on quantum many-body systems.

Information geometry is a powerful tool to study QSLs. In this setting, one finds a general framework providing an infinite family of QSLs based on contractive Riemannian metrics on the space of quantum states, which applies to any physical process[29]. In this scenario, the QSL relates to a certain information-theoretic distinguishability measure built for a set of quantum states, pure or mixed, separable or entangled, valid for closed and open systems. In addition, QSL bounds were investigated theoretically using matrix norms, e.g., Schatten p-norms, applied to the generator of the nonunitary dynamics[30–33]. Recent results include the study of bounds on the speed of observables related to open quantum systems[34], and also the proposal of a general framework for deriving tighter speed limits for macroscopic systems[35], which in turn finds applications in transport phenomena and nonequilibrium dynamics in spin systems.

[1]Departamento de Física, Universidade Federal do Maranhão, Campus Universitário do Bacanga, São Luís, Maranhão, Brazil. [2]Instituto de Física de São Carlos, Universidade de São Paulo, São Carlos, São Paulo, Brazil. [3]Quantum Research Center, Technology Innovation Institute, Abu Dhabi, UAE. [4]Instituto de Química, Universidade Federal Fluminense, Outeiro de São João Batista, Niterói, RJ, Brazil. [5]Instituto de Física, Universidade Federal do Rio de Janeiro, Rio de Janeiro, RJ, Brazil. ✉e-mail: frederico.brito@tii.ae

In the last years, several works include an analysis of QSLs for driven quantum systems under Markovian evolution[7,36]. These results triggered studies of QSLs for particular choices of quantum channels focusing on how the degree of non-Markovianity could affect the tightness of QSL bounds[37–41]. Overall, non-Markovian dynamics present an intricate physical structure, allowing the revivals of genuine quantum resources during the evolution, for example, quantum coherence, thus contrasting with the typical monotonic loss observed in Markovian scenarios[42]. In ref. 43, the authors discussed timescales related to generate an amount of quantumness under arbitrary physical process, also investigating the dependence of the QSL bound on initial and final states, and the role played by non-Markovian effects. Noteworthy, QSL depends on the initial state and the dynamical map governing the system evolution, showing the absence of a general connection between non-Markovianity and the speed of evolution of a quantum system[44–47].

Recently, an experimental measurement of the QSL time in a trapped single-atom system showed a crossover between the Mandelstam-Tamm and Margolus-Levitin bounds, with the latter dominating the dynamics for longer times[48]. We also mention the experimental discussion of the MT bound for time-dependent Hamiltonians with nuclear spin systems[49]. Despite all theoretical advances in understanding QSLs and experimental achievements for closed quantum systems, the field still lacks experimental studies exploring and certifying the machinery developed for open quantum systems. That happens due to the challenge of controlling the system-environment interaction and configuration, which determines the Markovian or non-Markovian character of the evolution.

In this work, we assess geometric QSLs in an open quantum system, by controlling just two parameters of the bath: the relaxation times of the hydrogen and carbon nuclear spins of an ensemble of chloroform molecules in a liquid-state Nuclear Magnetic Resonance (NMR) experiment. We control the relaxation rates of the carbon and hydrogen nuclear spins by adding a paramagnetic salt to the solution, allowing us to observe the transition from non-Markovian to Markovian regimes in the dynamics[50,51]. Then, we investigate how the speed of evolution is affected under different experimental conditions. For non-Markovian dynamics and low salt concentrations, we observe crossovers between quantum speed limits defined by the quantum Fisher information and the Wigner-Yanase skew information metrics. The occurrence of these crossovers is related to the character of the systems time evolution. In high concentrations, the Wigner-Yanase metric sets the tighter quantum speed limit bound when the system undergoes non-Markovian or Markovian dynamics.

Results

Quantum speed limits for open system dynamics

The quantum speed limit (QSL) is related to the distinguishability of quantum states from a geometric perspective[29]. We remind that the so-called Morozova-Čencov-Petz (MCP) theorem states that the convex space of quantum states is endowed with a family of contractive Riemannian metrics[52,53]. In this sense, the nonuniqueness of distinguishability measures of quantum states implies a class of geometric QSLs that can be exploited in the search for tighter bounds. Here, we discuss the QSL time for the single-qubit state ρ_t in Eq. (7). The evolution of this state draws a path γ in the space of quantum states connecting initial ρ_0 and final ρ_τ states. The MCP theorem states that the length $\ell_\gamma^f(\rho_0,\rho_\tau)$ of such path depends on some chosen contractive Riemannian metric related to a given Morozova-Čencov (MC) function f[52,53]. Hereafter, we will restrict our analysis to two paradigmatic metrics: the quantum Fisher information (QFI) and the Wigner-Yanase skew information (WY). In particular, focusing on the single-qubit state in Eq. (7), the length of the path depicted by the nonunitary evolution of the state ρ_t becomes

$$\ell_\gamma^f(\rho_0,\rho_\tau)=\frac{1}{2}\int_0^\tau dt\sqrt{h_t^f}\left|\frac{d\langle\sigma_x\rangle_t}{dt}\right|, \tag{1}$$

with

$$h_t^{\mathrm{QFI}}:=\frac{1-\langle\sigma_z\rangle_0^2}{1-\langle\sigma_x\rangle_t^2-\langle\sigma_z\rangle_0^2}, \tag{2}$$

and

$$h_t^{\mathrm{WY}}:=\frac{\langle\sigma_x\rangle_t^2}{\left(\langle\sigma_x\rangle_t^2+\langle\sigma_z\rangle_0^2\right)\left(1-\langle\sigma_x\rangle_t^2-\langle\sigma_z\rangle_0^2\right)}+\frac{2\langle\sigma_z\rangle_0^2\left(1-\sqrt{1-\langle\sigma_x\rangle_t^2-\langle\sigma_z\rangle_0^2}\right)}{\left(\langle\sigma_x\rangle_t^2+\langle\sigma_z\rangle_0^2\right)^2}. \tag{3}$$

Overall, the quantity $(1/2)\sqrt{h_t^f}|d\langle\sigma_x\rangle_t/dt|$ in Eq. (1) signals the speed of evolution respective to the nonunitary dynamics of the single-qubit state, for a given Riemannian metric. Note that this quantity depends on the time-dependent single-qubit observable $\langle\sigma_x\rangle_t$ that is accessed experimentally. For details in the proof of Eqs. (1), (2), and (3), see the Supplementary Note 1, and also refs. 29,52–55 therein. We point out that γ is an arbitrary path connecting states ρ_0 and ρ_τ, and its length need not be the shortest one[56]. Indeed, for a given Riemannian metric on the space of quantum states, there exists a geodesic path with minimum length $\mathcal{L}^f(\rho_0,\rho_\tau)$ followed by the evolved state ρ_t when going from ρ_0 to ρ_τ. On the one hand, the geodesic length related to the QFI metric is given by the Bures angle, $\mathcal{L}^{\mathrm{QFI}}(\rho_0,\rho_\tau)=\arccos[\sqrt{F(\rho_0,\rho_\tau)}]$, where the Uhlmann fidelity related to initial ρ_0 and final ρ_τ single-qubit states yields

$$F(\rho_0,\rho_\tau)=\frac{1}{2}\left[1+\langle\sigma_x\rangle_0\langle\sigma_x\rangle_\tau+\langle\sigma_z\rangle_0^2+\prod\nolimits_{s=0,\tau}\sqrt{1-\langle\sigma_x\rangle_s^2-\langle\sigma_z\rangle_0^2}\right]. \tag{4}$$

On the other hand, the WY metric implies the geodesic length known as Hellinger angle, $\mathcal{L}^{\mathrm{WY}}(\rho_0,\rho_\tau)=\arccos[A(\rho_0,\rho_\tau)]$, while the quantum affinity for single-qubit states is given by

$$A(\rho_0,\rho_\tau)=\frac{\langle\sigma_x\rangle_0\langle\sigma_x\rangle_\tau+\langle\sigma_z\rangle_0^2+\prod_{s=0,\tau}\left(1+\sqrt{1-\langle\sigma_x\rangle_s^2-\langle\sigma_z\rangle_0^2}\right)}{\prod_{s=0,\tau}\left(\sqrt{1+\sqrt{\langle\sigma_x\rangle_s^2+\langle\sigma_z\rangle_0^2}}+\sqrt{1-\sqrt{\langle\sigma_x\rangle_s^2+\langle\sigma_z\rangle_0^2}}\right)}. \tag{5}$$

The geodesic length constitutes a lower bound for the length of the path drawn by the above dynamical evolution, i.e., $\mathcal{L}^f(\rho_0,\rho_\tau)\le\ell_\gamma^f(\rho_0,\rho_\tau)$. Solving this inequality as a function of time, one finds the QSL time related to the nonunitary evolution of the single-qubit state in Eq. (7). In this setting, any distinguishability measure of quantum states gives rise to a different geometric QSL. The contractive Riemannian metric whose geodesic length $\mathcal{L}^f$ is effectively tailored to the nonunitary dynamical evolution depicted by the length ℓ_γ^f is the one that signals the tightest QSL[29]. To investigate the tightness of a given geometric QSL, we set the relative deviation

$$\delta_\gamma^f:=\frac{\ell_\gamma^f(\rho_0,\rho_\tau)-\mathcal{L}^f(\rho_0,\rho_\tau)}{\mathcal{L}^f(\rho_0,\rho_\tau)}. \tag{6}$$

For a given metric, Eq. (6) indicates how far the dynamical evolution is from the respective geodesic path, and is expected to approach zero when both coincide such that the QSL bound saturates. Here, the tightest geometric QSL for the nonunitary dynamics of the single-qubit state is obtained after minimizing the quantity δ_γ^f over the two aforementioned information-theoretic quantifiers, namely, QFI and WY metrics. In addition, we consider the relative difference $\delta_\gamma^{\mathrm{QFI}}-\delta_\gamma^{\mathrm{WY}}$ as a criterion to testify the tightest QSL, i.e., for $\delta_\gamma^{\mathrm{QFI}}-\delta_\gamma^{\mathrm{WY}}>0$ we have that WY metric assigns the tighter QSL, while for $\delta_\gamma^{\mathrm{QFI}}-\delta_\gamma^{\mathrm{WY}}<0$ the QFI metric sets the tightest lower bound.

In the following, we discuss geometric QSLs for the single-qubit state by focusing on QFI and WY metrics. To do so, we compare numerical simulations of the open-system dynamics with the results calculated using experimental data. The quantum state undergoes a nonunitary evolution exhibiting both non-Markovian and Markovian regimes. In the limit of high concentrations in which the system undergoes Markovian dynamics, we find that the WY metric sets the tighter QSL bound. However, for low concentrations, we observe non-Markovian dynamics, and the relative difference $\delta_\gamma^{\mathrm{QFI}} - \delta_\gamma^{\mathrm{WY}}$ [see Eq. (6)] exhibits crossovers between the geometric QSL bounds related to the QFI and WY metrics.

Control of longitudinal and transverse relaxation times

In our experiments, we consider a two-qubit system encoded on the nuclear spins of the ^{13}C and ^{1}H of an ensemble of chloroform ($CHCl_3$) molecules in liquid-state at room temperature. The interaction between the spins is given by the Hamiltonian $H = \frac{\pi J}{2}\sigma_z \otimes \sigma_z$, where J is the strength of the interaction, and σ_i is the i-th Pauli matrix ($i = x, y, z$). For simplicity, we set $\hbar = 1$. The non-unitary dynamics for each nuclear spin are described by the longitudinal and transverse relaxation times, $T_{1,(C,H)}$ and $T_{2,(C,H)}$, respectively. The longitudinal relaxation time is associated with the spin-lattice relaxation, i.e., the return of the system to thermal equilibrium. The transverse relaxation time describes the spin-spin relaxation, which affects only the coherences of the density matrix. In Fig. 1(a), we show the long decay of the ^{13}C FID when we decouple the ^{13}C and ^{1}H nuclear spins, which makes clear the effect of the ^{1}H as the main source of decoherence. This effect happens due to the longitudinal relaxation of the ^{1}H nuclear spin and the scalar J coupling having the same time scale. When $T_{1,H} \approx 1/J$, the random spin flips on the proton spin caused by the $T_{1,H}$ process make the scalar interaction effectively time-dependent, turning the ^{1}H into a source of decoherence for the ^{13}C. Thus, by changing the concentration of $Fe(acac)_3$, we control the correlation time of the system-environment interaction (see further details in the Methods).

In the presence of paramagnetic ions, the magnetic dipolar interaction of the nuclear spins with the spins of the ion's unpaired electrons is usually much stronger than with other nuclear spins. Thus paramagnetic relaxation becomes the primary nuclear relaxation mechanism, scaling up the inverse of the average distance between the ions and the nucleus, resing in a linear dependence of the relaxation rates, $1/T_{1,H}$ and $1/T_{2,C}$, with the concentration of paramagnetic ions[57]. Figure 1b, c show the linear behavior for $1/T_{1,H}$ and $1/T_{2,C}$, as expected for paramagnetic relaxation.

Geometric QSL bounds

In Fig. 2, we present the tightness of the geometric QSL bounds related to QFI and WY metrics, and the Markovian/non-Markovian properties of the nonunitary dynamics of the single-qubit system. The solid lines depict the best fit using the model given in Eq. (7). The system initiates at the state $\rho_0 = (1/2)(\mathbb{I} + (\sigma_x + \sigma_z)/\sqrt{2})$. The measured values are $T_{1,H} = 12 \pm 1$ ms and $T_{2,C} = 480 \pm 20$ ms for $C = 20$ mM; $T_{1,H} = 1.7 \pm 0.2$ ms and $T_{2,C} = 87 \pm 3$ ms for $C = 120$ mM; and $T_{1,H} = 0.63 \pm 0.08$ ms and $T_{2,C} = 29 \pm 2$ ms for $C = 300$ mM. In the numerical simulations, we used the coupling strength $J = 209.1$ Hz, with $T_{1,H} = 7.1$ ms and $T_{2,C} = 38.55$ ms for $C = 20$ mM [see panels a, d, g, and j in Fig. 2]; $T_{1,H} = 1.15$ ms and $T_{2,C} = 12.8$ ms for $C = 120$ mM [see panels b, e, h, and k in Fig. 2]; and $T_{1,H} = 0.425$ ms and $T_{2,C} = 5.49$ ms for $C = 300$ mM [see panels c, f, i, and l in Fig. 2]. The large discrepancy between the measured and simulated values is mainly due to frequency offset errors, which accelerate the signal decay and lead to shorter $T_{1,H}$ and $T_{2,C}$ for fitted values. Such errors come from difficulty in setting the exact resonance frequency when the spectral lines are broad due to the fast relaxation rates used in the experiments. Despite this, note that the measured and simulated values for $T_{1,H}$ have the same order of magnitude. For the physical model in Eq. (8), the relaxation time $T_{1,H}$ is more relevant than $T_{2,C}$. To see this, first we note that $T_{1,H}/T_{2,C} \ll 1$, i.e., the function $\xi(t)$ [see Eq. (8)] will be mainly dominated by $T_{1,H}$ rather than $T_{2,C}$.

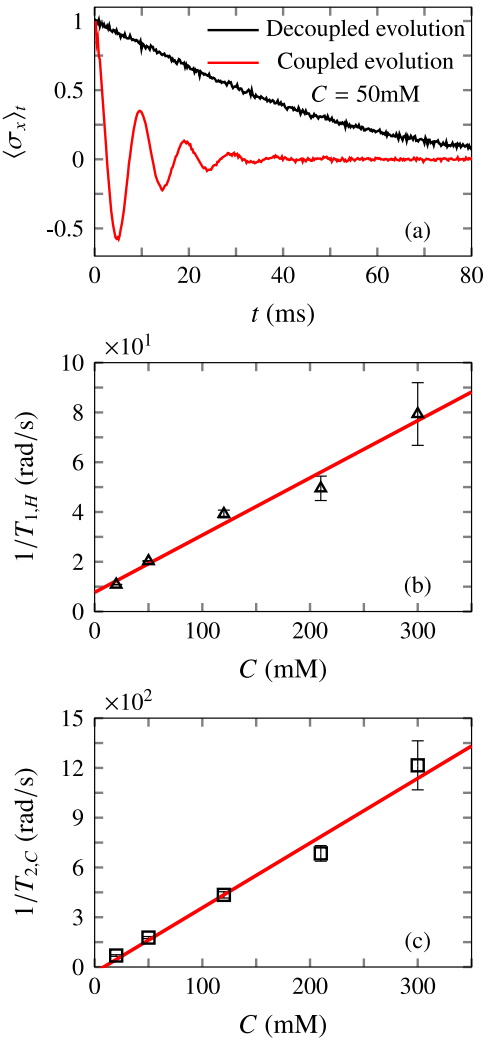

Fig. 1 | Couple-decoupled ^{13}C evolution, and Longitudinal and transverse relaxation times. a Coupled (red points) and decoupled (black points) ^{13}C FID's for the 50 mM concentration, showing the speedup of the decoherence due to scalar relaxation. The deviation from an exponential decay is the result of a small frequency offset. **b** and (**c**) The dependence of $T_{1,H}$ (triangles) and $T_{2,C}$ (squares) on the $Fe(acac)_3$ concentration, exhibiting the well known linear dependence of the relaxation rate on the concentration of a paramagnetic species[57]–red lines indicate the best linear fit of the data. Error bars for T_2 are the standard deviations from the fits of the decoupled FIDs for each concentration. For T_1, the error bars are calculated from the error propagation of the parameter t_1 in the inversion recovery sequence. The error in t_1 is obtained experimentally, checking the small range of t_1 values with a similar NMR signal.

Discussion

In the following, we comment on the non-Markovian and Markovian dynamical signatures of the quantum system. The characterization of non-Markovian dynamics has motivated several efforts to understand the mechanism of information backflow from the environment to the system, and the notion of divisibility of a dynamical map. Historically, the study of information backflow in open quantum systems with the set of measures of non-Markovianity introduced by (i) Breuer, Laine, and Piilo (BLP)[58]; (ii) Rivas, Huelga, and Plenio (RHP)[59]; (iii) Luo, Fu, and Song (LFS)[60]. In spite of that, recent studies have addressed the dynamical behavior of quantum coherence measures to characterize non-Markovianity[61–63]. For a single qubit dissipative channel, it has been shown that the ℓ_1-norm of coherence exhibits revivals and thus captures non-Markovian signatures of the dynamics in the same way as the BLP measure[64]. The main idea is that, since

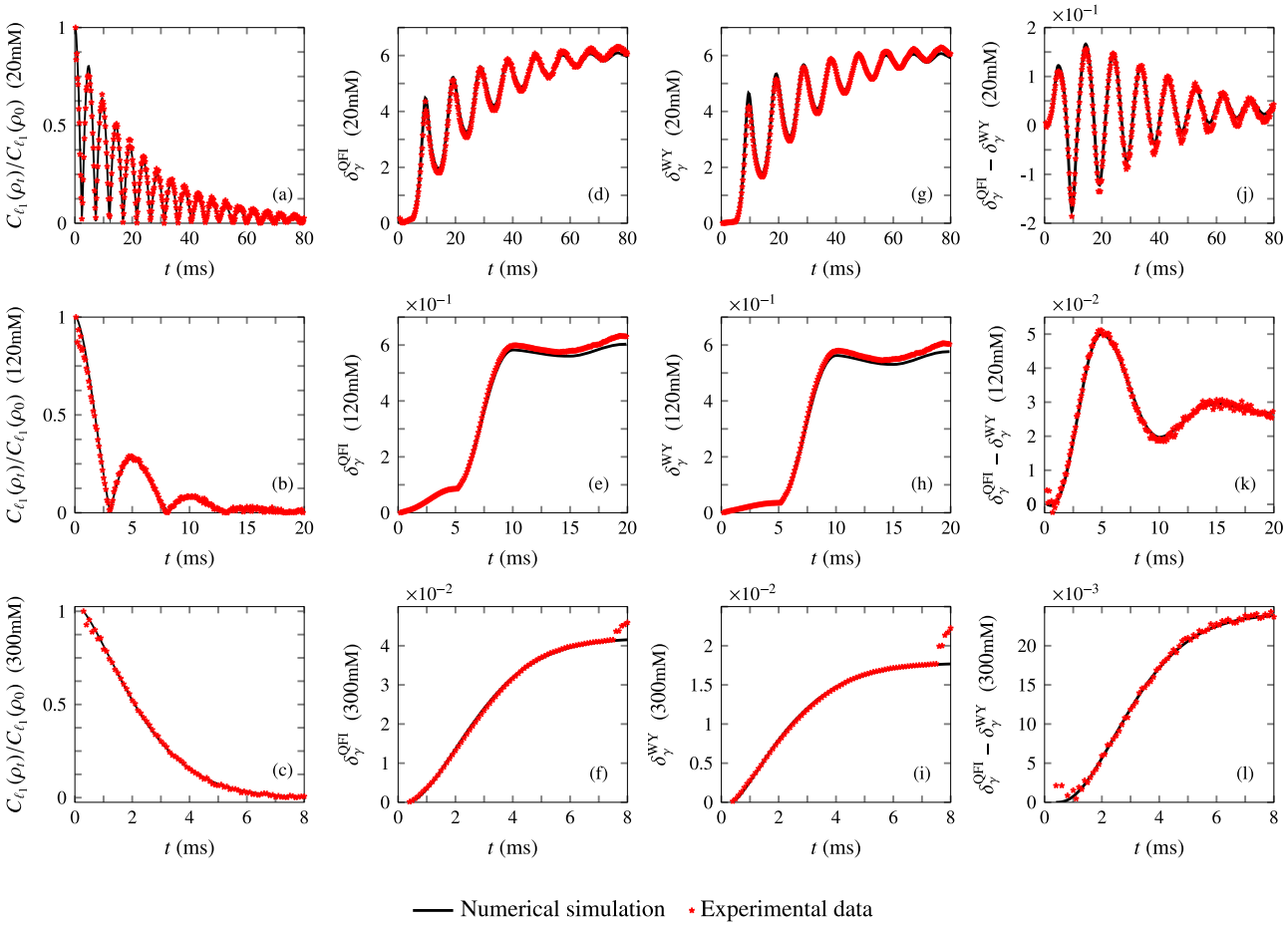

Fig. 2 | Coherence measure and geometric QSL bounds. Numerical simulation (black line) and experimental data (red dots) plots of the normalized coherence measure $C_{\ell_1}(\rho_t)/C_{\ell_1}(\rho_0)$ (**a**–**c**) relative deviations for quantum Fisher information $\delta_\gamma^{\mathrm{QFI}}$ (**d**–**f**) and Wigner-Yanase skew information metrics $\delta_\gamma^{\mathrm{WY}}$ (**g**–**i**), and relative difference $\delta_\gamma^{\mathrm{QFI}} - \delta_\gamma^{\mathrm{WY}}$ (**j**–**l**) for the concentrations 20 mM (**a**, **d**, **g**, and **j**), 120 mM (**b**, **e**, **h**, and **k**) and 300 mM (**c**, **f**, **i**, and **l**). The system is initialized at the single-qubit state $\rho_0 = (1/2)(\mathbb{I} + \langle\sigma_x\rangle_0\sigma_x + \langle\sigma_z\rangle_0\sigma_z)$, with $\langle\sigma_x\rangle_0 = \langle\sigma_z\rangle_0 = 1/\sqrt{2}$. The following parameters were used for the numerical simulations setting the coupling strength $J = 209.1$ Hz, with $T_{1,H} = 7.1$ ms and $T_{2,C} = 38.55$ ms (**a**, **d**, **g**, and **j**); $T_{1,H} = 1.15$ ms and $T_{2,C} = 12.8$ ms (**b**, **e**, **h**, and **k**); $T_{1,H} = 0.425$ ms and $T_{2,C} = 5.49$ ms (**c**, **f**, **i**, and **l**).

the coherence measure monotonically decreases under completely positive and trace preserving (CPTP) incoherent operations, one finds the ℓ_1-norm of coherence useful for detecting non-Markovianity. For a detailed discussion, see ref. 65 and references therein. In this setting, we investigate the dynamical behavior of quantum coherence of the two-level system, thus characterizing non-Markovian and Markovian regimes based on the so-called ℓ_1-norm of coherence. Panels a–c in Fig. 2 show the normalized ℓ_1-norm of coherence of the evolved single-qubit state for different concentrations of $Fe(acac)_3$, with $C_{\ell_1}(\rho_t) = \sum_{j\neq l}|\langle j|\rho_t|l\rangle|$[66,67]. Here, we set $\{|0\rangle, |1\rangle\}$ as the reference basis to evaluate the coherence measure, with $\sigma_z|s\rangle = (-1)^s|s\rangle\ \forall s \in \{0, 1\}$. In Fig. 2a, with $C = 20$ mM, the normalized quantum coherence measure exhibits periodic revivals with damped amplitudes, thus vanishing at later times of the dynamics. Figure 2b shows a qualitatively similar behavior, with the quantum coherence approaching zero faster for $C = 120$ mM. In both cases, the revivals point to the signature of non-Markovian dynamics. In Fig. 2c, the quantum coherence displays a monotonic decay for $C = 300$ mM, a typical behavior of Markovian dynamics[58,64,65]. Overall, from low to high concentrations of the paramagnetic salt, we observe the non-Markovian regime for $T_{1,H} \approx 1/J$ (20 mM and 120 mM), while for $T_{1,H} \ll 1/J$ the dynamics is Markovian (300mM).

Hereafter, we discuss the relative deviation δ_γ^f [see Eq. (6)] for the geometric QSL bound constructed with the QFI metric [panels d, e, and f in Fig. 2], and the WY metric [panels g, h, and i in Fig. 2]. These quantities are very sensitive to noise since even the small fluctuations observed for short times in the signals of 120 and 300 mM concentrations heavily affect δ_γ^f. This happens due to the time-derivative in Eq. (1). Thus, to avoid undesired numerical errors, we smoothed the data before the numerical integration to evaluate ℓ_γ^f for both metrics. The results without smoothing the data are shown in Supplementary Note 1. Panels d and g in Fig. 2 show the relative deviations $\delta_\gamma^{\mathrm{QFI}}$ and $\delta_\gamma^{\mathrm{WY}}$ within the non-Markovian regime of the dynamics, with $C = 20$ mM. These relative deviations oscillate out of phase with the FID signal. Next, for $C = 120$ mM, panels e and h in Fig. 2 show each relative deviation with a non-monotonic behavior, a fingerprint of non-Markovianity for non-unitary evolution. Panels f and i in Fig. 2 show that for $C = 300$ mM, both relative deviations behave monotonically as a function of the evolution time of the Markovian dynamics.

To investigate the tightness of the quantum speed limit, we plot in panels j, k, and l in Fig. 2 the relative difference $\delta_\gamma^{\mathrm{QFI}} - \delta_\gamma^{\mathrm{WY}}$ for the concentrations 20 mM,120 mM and 300 mM, respectively. Importantly, for $\delta_\gamma^{\mathrm{QFI}} - \delta_\gamma^{\mathrm{WY}} > 0$, one finds the tighter speed limit signaled by the WY metric. Otherwise, for $\delta_\gamma^{\mathrm{QFI}} - \delta_\gamma^{\mathrm{WY}} < 0$, the QFI metric systematically produces the tightest lower bound to the evolution time. It is worth noting that the tightness of the QSL bound depends on the physical process considered. It turns out that the QSL bound related to the QFI metric is tighter than that speed limit obtained from WY metric for closed quantum systems[29]. However, our experiments show the opposite situation for the considered open quantum system dynamics. For $C = 20$ mM, Fig. 2j shows that the relative difference oscillates over the evolution time and exhibits crossovers between $\delta_\gamma^{\mathrm{QFI}}$ and $\delta_\gamma^{\mathrm{WY}}$, and both QFI and WY metrics give rise to the same geometric QSL whenever $\delta_\gamma^{\mathrm{QFI}} - \delta_\gamma^{\mathrm{WY}} = 0$. No crossover occurs after

$t \sim 57.4$ ms, and the QSL related to the WY metric turns out to be the tighter one at later times of the dynamics. The tightest geometric QSL is captured by the Wigner-Yanase skew information metric for the two higher concentrations, even for the non-Markovian regime observed for the 120 mM concentration. This is seen in panels k and l in Fig. 2.

Conclusions

In summary, we experimentally assess geometric speed limits for the nonunitary dynamics of a qubit encoded on ^{13}C nuclear spin. We control the relaxation rates of the qubit by adding $Fe(acac)_3$ to the solution. The paramagnetic relaxation makes it possible to vary the relaxation times by two orders of magnitude, and we could observe a transition between non-Markovian to Markovian regimes in the nonunitary reduced dynamics of ^{13}C spins depending on the salt concentrations. Taking a geometric approach to address the QSL based on the quantum Fisher information (QFI) and Wigner-Yanase (WY) skew information metrics, we find a good agreement between the results of numerical simulations and the experiment. We emphasize the tightness of the QSL depends on the properties of the physical process that is considered, i.e., it is a function of the initial state and the dynamical map that governs the system evolution. For example, for any single-qubit unitary dynamics, it is known that the geometric QSL related to the QFI metric is tighter than the one corresponding to the WY metric. However, one can find instances of nonunitary dynamics of single-qubit states in which the QSL bound constructed with the WY metric is tighter than the QFI one, and vice-versa[29].

The present work is novel in the specialized literature, as it discusses the experimental investigation of QSLs for an open quantum system carried out on a controllable Nuclear Magnetic Resonance platform. Past results covered experimental discussion of the QSL derived by Mandelstam-Tamm for the unitary dynamics of nuclear spin systems[49], and also the study of the Mandestam-Tamm and Margolus-Levitin speed limits by using the technique of matter wave interferometry of single atom in an optical trap[48]. Our discussion focuses on geometric QSLs related to the QFI and WY metrics. To the best of our knowledge, QFI and WY metrics cannot be directly measured for general physical processes. It is known that these quantities recover the variance of the dynamical generator for closed systems initialized at pure states[68,69]. However, for nonunitary dynamics and mixed states, bounds on the variance are found that provide, at most, estimates of these quantities[70,71]. To overcome such issues, we recast the geometric QSL bounds in terms of single-qubit observables $\{\langle\sigma_l\rangle_{0,t}\}_{l=x,y,z}$ [see Eqs. (1)–(5)], which are probed experimentally.

In our physical system, we find that the tightness of the QSL bound is somehow related to the concentration of the paramagnetic salt that is added to the ensemble of chloroform molecules. By varying such concentration, the strength of the system-reservoir coupling changes and therefore a transition between non-Markovian to Markovian regimes is observed in the single-qubit dynamics encoded in nuclear carbon spins. For lower concentrations ($C = 20$ mM), we observe crossovers between the QFI and WY as the tighter one on a non-Markovian regime. In the other two studied cases ($C = 120$ mM and $C = 300$ mM), the WY metric sets the tighter QSL, both in non-Markovian and Markovian dynamics.

We remark how geometric QSLs are very sensitive to noise, i.e., even tiny fluctuations observed for short times in the data, from low to high concentrations, heavily affect the figure of merit that signals the tighter QSL bound of the two-level system. We note that the relative deviation indicates how much the dynamical evolution differs from the respective geodesic related to the considered metric. The smaller the relative deviation, the tighter the QSL bound for each concentration. We note that the relative deviations $\delta_\gamma^{\mathrm{QFI}}$ and $\delta_\gamma^{\mathrm{WY}}$ show similar numerical behaviors for each concentration [see panels d-i in Fig. 2]. This means that, for the physical process considered, the QFI and WY metrics provide QSL bounds that are close to each other. Finally, this result might suggest that neither QFI or WY metrics can be the fundamental one, which can foster the investigation of new proposals of bona fide QSL metrics.

Methods

System dissipative dynamics

In our experiments, the two-qubit system initiates in a thermal equilibrium state $\rho_T^{CH} \approx [(1-\epsilon_C)/4]\,\mathbb{I}\otimes\mathbb{I} + (\epsilon_C/2)\,|0\rangle\langle 0|\otimes\mathbb{I} + (\epsilon_H/4)\,\mathbb{I}\otimes\sigma_z$, which is valid at the high-temperature limit ($\epsilon_l \ll 1$), with $\epsilon_l = \hbar\omega_l/k_BT$ and $\omega_{C,H}$ is the ^{13}C (^{1}H) Larmor frequency, k_B is the Boltzmann constant, and T is the temperature. Since we are interested in the ^{13}C magnetization, one can discard the first and third terms in state ρ_T^{CH}, such that the density matrix for the ^{13}C spin is given, up to normalization, by $\rho^C = \mathrm{Tr}_H(\rho_T^{CH}) \approx |0\rangle\langle 0|$[50]. We obtain the initial state for our experiments after a $\pi/4$ rotation on the y-axis, resulting in $\rho_0^C = (1/2)(\mathbb{I} + (\sigma_x + \sigma_z)/\sqrt{2})$. To model the open system dynamics of the carbon nuclear spin, we followed the description in refs. 50,72. The decoherence for each nuclear spin is described by the longitudinal and transverse relaxation times, $T_{1,(C,H)}$ and $T_{2,(C,H)}$, respectively. The longitudinal relaxation time is associated to the spin-lattice relaxation, i.e., the return of the system to thermal equilibrium. The transverse relaxation time describes the spin-spin relaxation, which affects only the coherences of the density matrix.

In our system, the ^{1}H spin becomes a source of the decoherence for the carbon spin when the condition $T_{1,H} \approx 1/J$ is satisfied. Under this condition, the flips on the proton spin due to $T_{1,H}$ occur at the same time scale as the evolution caused by the scalar coupling, introducing an effective time dependence on this coupling. This results in a faster decay of the system magnetization, known as scalar relaxation[57]. This process is inhomogeneous in time, with a correlation time given by the minimum between $T_{1,H}$ and $1/J$[50,72,73]. By modulating $T_{1,H}$ through paramagnetic relaxation, we can control the degree of non-Markovianity of the ^{13}C open-system dynamics. In the limit of fast correlation time, $T_{1,H} \ll 1/J$, i.e., for high concentrations of the paramagnetic salt, we observe Markovian dynamics for the system dephasing.

We consider a phase-damping channel to model the spin-spin relaxation of the ^{13}C spin and a single bit-phase flip channel for both spin-lattice and spin-spin relaxations of the ^{1}H spin, since $T_{1,H} \approx T_{2,H}$ for all experimental configurations discussed throughout our results. The Kraus operators for the phase damping are $K_1 = \sqrt{q_t}\,\mathbb{I}\otimes\mathbb{I}$ and $K_2 = \sqrt{1-q_t}\,\sigma_z\otimes\mathbb{I}$, with $q_t = (1+e^{-t/2T_{2,C}})/2$. For the bit-phase flip, one gets $\mathcal{E}_1 = \sqrt{p_t}\,\mathbb{I}\otimes\mathbb{I}$ and $\mathcal{E}_2 = \sqrt{1-p_t}\,\mathbb{I}\otimes\sigma_y$, where $p_t = (1+e^{-t/2T_{1,H}})/2$. Here $T_{1,H}$ and $T_{2,C}$ define the characteristic time of the bit-phase flip channel and phase damping channel, respectively.

In this scenario, the state of the two-qubit system during the evolution is obtained by the application of the Kraus operators to the initial state, when partitioning the evolution time $0 \le t \le \tau$ into N equal steps of size $\Delta t = \tau/N$, with $J\Delta t \ll 1$. Hence, by iterating such a process, with $\Delta t \to 0$ ($N \to \infty$), and tracing out the hydrogen degrees of freedom, one obtains the single-qubit marginal state as follows

$$\rho_t^C = \frac{1}{2}\left(\mathbb{I} + \langle\sigma_x\rangle_t\,\sigma_x + \langle\sigma_z\rangle_0\,\sigma_z\right), \tag{7}$$

where $\langle\sigma_x\rangle_t = \xi(t)\,\langle\sigma_x\rangle_0$ stands for the transversal magnetization of the ^{13}C (hereafter the system), with

$$\xi(t) = e^{-t/2T_{2,C}}e^{-t/4T_{1,H}}\left[\frac{t}{4T_{1,H}}\,\mathrm{sinc}\left(\frac{t}{4T_{1,H}}\sqrt{16\pi^2J^2T_{1,H}^2-1}\right) + \cos\left(\frac{t}{4T_{1,H}}\sqrt{16\pi^2J^2T_{1,H}^2-1}\right)\right], \tag{8}$$

with $\mathrm{sinc}(x) := \sin x/x$, and $\xi(0) = 1$. For more details, see the Supplementary Note 2. From now on, we will omit the superscript in Eq. (7) and define ρ_t as the single-qubit state of the ^{13}C nuclear spin.

The function $\xi(t)$ in Eq. (8) encodes the nonunitary signatures in the dynamics of the two-level system. Furthermore, it shows how reducing $T_{1,H}$ increases the role of the ^{1}H nuclear spin as the main source of decoherence, with the dynamics dominated by the sinc(•) term in Eq. (8) and the oscillations due to the scalar interaction disappearing for $T_{1,H} \ll 1/J$. Thus, to evaluate the geometric QSL of a given Riemannian metrics, we prepare the state ρ_0 by the application of a single $(\pi/4)$ pulse on the y-axis and let the system evolve according to Eq. (8). We control the relaxation rates $1/T_{1,H}$ and $1/T_{2,C}$ by adding the paramagnetic salt iron(III) acetylacetonate ($Fe(acac)_3$) to the solution, with the relaxation rates growing linearly with the concentration of $Fe(acac)_3$[57].

Experimental setup

We carried out the measurements at 25° C in a Bruker Avance III 600 MHz, with ^{1}H and ^{13}C Larmor frequencies of 600 and 150 MHz, respectively, with a 5 mm double resonance probe-head. We realized the experiments with a solution of chloroform ($CHCl_3$), with natural abundance of ^{13}C in a 5. mm NMR tube, doped with Iron(III) acetylacetonate ($Fe(acac)_3$, Sigma Aldrich). To guarantee good frequency stability, we used the deuterium signal of acetone-d6 (Cambridge Isotopes Laboratories - Inc.) to lock the NMR signal. We avoided the undesired line broadening of the deuterium reference signal, due to the effects of the paramagnetic salt, putting the acetone-d6 in a 3 mm NMR tube, all inside the 5 mm tube.

We prepared the solutions of $CHCl_3$ and Iron(III) acetylacetonate diluting the paramagnetic salt in 2 ml of $CHCl_3$. To get the concentrations of 20, 50, 120, 300 and 450 mM, we used 14.5(1), 35.5(1), 85.1(1), 211.6(1) and 317.8(1) miligrams of $Fe(acac)_3$, respectively. The error on the concentrations is of 1 mM. Each sample contained 150 μl of doped $CHCl_3$ and 150 μl of acetone-d6.

We measured the spin-lattice relaxation time $T_{1,(H,C)}$ for ^{1}H and ^{13}C using a standard inversion-recovery pulse sequence. We estimate $T_{1,(H,C)}$ adjusting the time delay t_1 in the sequence such that the magnetization vanishes. Under this condition, we can calculate $T_{1,(H,C)}$ from the equation $T_1 = t_1/\ln(2)$. The ^{13}C spin-spin relaxation time $T_{2,C}$ is measured from the Free Induction Decay (FID) signal obtained when both spins are decoupled through a Waltz-64 heteronuclear decoupling sequence[74], with a decoupling $\pi/2$-pulse of 54 μs. We assumed $T_{2,C} \approx T^*_{2,C}$ due to a good shimming. Here, $T^*_{2,C}$ is the characteristic time for the FID decay and it differs from $T_{2,C}$ due to the effects of inhomogeneities in the static field B_0[57]. To avoid frequency offset effects on the estimation of $T_{2,C}$, the FID signals were fitted using a function $M_x(t) = M_0\, e^{-t/T_{2,C}} \cos(\omega t)$, where M_0 is the initial magnetization amplitude and ω is the frequency offset. We used the spectrum of the thermal equilibrium state to adjust the phase and normalize the intensity of all NMR data throughout this work.

Data availability

The data that support the findings of this study are available from the corresponding author upon reasonable request.

Code availability

The code used for the analysis is available from the corresponding author upon reasonable request.

Received: 31 August 2023; Accepted: 17 April 2024;
Published online: 02 May 2024

References

1. Aharonov, Y. & Bohm, D. Time in the quantum theory and the uncertainty relation for time and energy. *Phys. Rev.* **122**, 1649 (1961).
2. Pfeifer, P. & Fröhlich, J. Generalized time-energy uncertainty relations and bounds on lifetimes of resonances. *Rev. Mod. Phys.* **67**, 759 (1995).
3. Mandelstam, L. & Tamm, I. in *Selected Papers* (eds Bolotovskii, B. M., Frenkel, V. Y. & Peierls, R.) 115–123 (Springer, 1991).
4. Margolus, N. & Levitin, L. B. The maximum speed of dynamical evolution. *Physica. D.* **120**, 188 (1998).
5. Taddei, M. M., Escher, B. M., Davidovich, L. & de Matos Filho, R. L. Quantum speed limit for physical processes. *Phys. Rev. Lett.* **110**, 050402 (2013).
6. del Campo, A., Egusquiza, I. L., Plenio, M. B. & Huelga, S. F. Quantum speed limits in open system dynamics. *Phys. Rev. Lett.* **110**, 050403 (2013).
7. Deffner, S. & Lutz, E. Quantum speed limit for non-markovian dynamics. *Phys. Rev. Lett.* **111**, 010402 (2013).
8. Okuyama, M. & Ohzeki, M. Quantum speed limit is not quantum. *Phys. Rev. Lett.* **120**, 070402 (2018).
9. Campaioli, F., Pollock, F. A. & Modi, K. Tight, robust, and feasible quantum speed limits for open dynamics. *Quantum* **3**, 168 (2019).
10. O'Connor, E., Guarnieri, G. & Campbell, S. Action quantum speed limits. *Phys. Rev. A* **103**, 022210 (2021).
11. Lokutsievskiy, L. & Pechen, A. Reachable sets for two-level open quantum systems driven by coherent and incoherent controls. *J. Phys. A: Math. Theor.* **54**, 395304 (2021).
12. Impens, F., D'Angelis, F. M., Pinheiro, F. A. & Guéry-Odelin, D. Time scaling and quantum speed limit in non-Hermitian Hamiltonians. *Phys. Rev. A* **104**, 052620 (2021).
13. Mohan, B., Das, S. & Pati, A. K. Quantum speed limits for information and coherence. *New J. Phys.* **24**, 065003 (2022).
14. Campaioli, F., Yu, C.-S., Pollock, F. A. & Modi, K. Resource speed limits: maximal rate of resource variation. *New J. Phys.* **24**, 065001 (2022).
15. Pires, D. P. Unified entropies and quantum speed limits for nonunitary dynamics. *Phys. Rev. A* **106**, 012403 (2022).
16. Ness, G., Alberti, A. & Sagi, Y. Quantum speed limit for states with a bounded energy spectrum. *Phys. Rev. Lett.* **129**, 140403 (2022).
17. Fogarty, T., Deffner, S., Busch, T. & Campbell, S. Orthogonality catastrophe as a consequence of the quantum speed limit. *Phys. Rev. Lett.* **124**, 110601 (2020).
18. Shao, Y., Liu, B., Zhang, M., Yuan, H. & Liu, J. Operational definition of a quantum speed limit. *Phys. Rev. Res.* **2**, 023299 (2020).
19. Puebla, R., Deffner, S. & Campbell, S. Kibble-Zurek scaling in quantum speed limits for shortcuts to adiabaticity. *Phys. Rev. Res.* **2**, 032020 (2020).
20. Kobayashi, K. & Yamamoto, N. Quantum speed limit for robust state characterization and engineering. *Phys. Rev. A* **102**, 042606 (2020).
21. Lam, M. R. et al. Demonstration of quantum brachistochrones between distant states of an atom. *Phys. Rev. X* **11**, 011035 (2021).
22. del Campo, A. Probing quantum speed limits with ultracold gases. *Phys. Rev. Lett.* **126**, 180603 (2021).
23. Mohan, B. & Pati, A. K. Reverse quantum speed limit: how slowly a quantum battery can discharge. *Phys. Rev. A* **104**, 042209 (2021).
24. Pires, D. P., Modi, K. & Céleri, L. C. Bounding generalized relative entropies: nonasymptotic quantum speed limits. *Phys. Rev. E* **103**, 032105 (2021).
25. Pires, D. P. & de Oliveira, T. R. Relative purity, speed of fluctuations, and bounds on equilibration times. *Phys. Rev. A* **104**, 052223 (2021).
26. Aghion, E. & Green, J. R. Thermodynamic speed limits for mechanical work. *J. Phys. A: Math. Theor.* **56**, 05LT01 (2023).
27. Hasegawa, Y. Unifying speed limit, thermodynamic uncertainty relation and heisenberg principle via bulk-boundary correspondence. *Nat. Commun.* **14**, 2828 (2023).
28. Gong, Z. & Hamazaki, R. Bounds in nonequilibrium quantum dynamics. *Int. J. Mod. Phys. B* **36**, 2230007 (2022).
29. Pires, D. P., Cianciaruso, M., Céleri, L. C., Adesso, G. & Soares-Pinto, D. O. Generalized geometric quantum speed limits. *Phys. Rev. X* **6**, 021031 (2016).
30. Deffner, S. & Campbell, S. Quantum speed limits: from heisenberg's uncertainty principle to optimal quantum control. *J. Phys. A: Math. Theor.* **50**, 453001 (2017).

31. Deffner, S. Geometric quantum speed limits: a case for wigner phase space. *New J. Phys.* **19**, 103018 (2017).
32. Rosal, A. J. B., Pires D. P. & Soares-Pinto, D. O. Quantum speed limits based on schatten norms. Preprint at https://arxiv.org/abs/2312.00533 (2023).
33. Wang, H. & Qiu, X. Generalized coherent quantum speed limits. Preprint at https://arxiv.org/abs/2401.01746 (2024).
34. García-Pintos, L. P., Nicholson, S. B., Green, J. R., del Campo, A. & Gorshkov, A. V. Unifying quantum and classical speed limits on observables. *Phys. Rev. X* **12**, 011038 (2022).
35. Hamazaki, R. Speed limits for macroscopic transitions. *PRX Quantum* **3**, 020319 (2022).
36. Lan, K., Xie, S. & Cai, X. Geometric quantum speed limits for markovian dynamics in open quantum systems. *New J. Phys.* **24**, 055003 (2022).
37. Xu, Z.-Y. & Zhu, S.-Q. Quantum speed limit of a photon under non-markovian dynamics. *Chinese Phys. Lett.* **31**, 020301 (2014).
38. Sun, Z., Liu, J., Ma, J. & Wang, X. Quantum speed limits in open systems: non-markovian dynamics without rotating-wave approximation. *Sci. Rep.* **5**, 8444 (2015).
39. Meng, X., Wu, C. & Guo, H. Minimal evolution time and quantum speed limit of non-markovian open systems. *Sci. Rep.* **5**, 16357 (2015).
40. Mirkin, N., Toscano, F. & Wisniacki, D. A. Quantum-speed-limit bounds in an open quantum evolution. *Phys. Rev. A* **94**, 052125 (2016).
41. Zhang, Y.-J., Xia, Y.-J. & Fan, H. Control of quantum dynamics: non-markovianity and the speedup of the open system evolution. *EPL (Europhysics Letters)* **116**, 30001 (2016).
42. Rivas, A., Huelga, S. F. & Plenio, M. B. Quantum non-markovianity: characterization, quantification and detection. *Rep. Prog. Phys.* **77**, 094001 (2014).
43. Jing, J., Wu, L.-A. & del Campo, A. Fundamental speed limits to the generation of quantumness. *Sci. Rep.* **6**, 38149 (2016).
44. Xu, Z.-Y., Luo, S., Yang, W. L., Liu, C. & Zhu, S. Quantum speedup in a memory environment. *Phys. Rev. A* **89**, 012307 (2014).
45. Cianciaruso, M., Maniscalco, S. & Adesso, G. Role of non-markovianity and backflow of information in the speed of quantum evolution. *Phys. Rev. A* **96**, 012105 (2017).
46. Teittinen, J., Lyyra, H. & Maniscalco, S. There is no general connection between the quantum speed limit and non-markovianity. *New J. Phys.* **21**, 123041 (2019).
47. Teittinen, J. & Maniscalco, S. Quantum speed limit and divisibility of the dynamical map. *Entropy* **23**, 331 (2021).
48. Ness, G. et al. Observing crossover between quantum speed limits. *Sci. Adv.* **7**, 9119 (2021).
49. Villamizar, D. V., Duzzioni, E. I., Leal, A. C. S. & Auccaise, R. Estimating the time evolution of NMR systems via a quantum-speed-limit–like expression. *Phys. Rev. A* **97**, 052125 (2018).
50. Kondo, Y., Matsuzaki, Y., Matsushima, K. & Filgueiras, J. G. Using the quantum zeno effect for suppression of decoherence. *New J. Phys.* **18**, 013033 (2016).
51. Ho, L. B., Matsuzaki, Y., Matsuzaki, M. & Kondo, Y. Nuclear magnetic resonance model of an entangled sensor under noise. *J. Phys. Soc. Japan* **89**, 054001 (2020).
52. Morozova, E. A. & Čencov, N. N. Markov invariant geometry on manifolds of states. *J. Sov. Math.* **56**, 2648 (1991).
53. Petz, D. Monotone metrics on matrix spaces. *Linear Algebra Appl.* **244**, 81 (1996).
54. Bengtsson, I. & Życzkowski, K. *Geometry of Quantum States: An Introduction to Quantum Entanglement* 1st edn (Cambridge University Press, 2006).
55. Nielsen, M. & Chuang, I. L. *Quantum Computation and Quantum Information: 10th Anniversary Edition* (Cambridge University Press, 2010).
56. Anandan, J. & Aharonov, Y. Geometry of quantum evolution. *Phys. Rev. Lett.* **65**, 1697 (1990).
57. Abragam, A. *The Principles of Nuclear Magnetism, International Series of Monographs on Physics*, Vol. 614 (Clarendon Press, 1961).
58. Breuer, H. P., Laine, E. M. & Piilo, J. Measure for the degree of non-markovian behavior of quantum processes in open systems. *Phys. Rev. Lett.* **103**, 210401 (2009).
59. Rivas, A., Huelga, S. F. & Plenio, M. B. Entanglement and non-markovianity of quantum evolutions. *Phys. Rev. Lett.* **105**, 050403 (2010).
60. Luo, S., Fu, S. & Song, H. Quantifying non-markovianity via correlations. *Phys. Rev. A* **86**, 044101 (2012).
61. Rivas, A. Refined weak-coupling limit: coherence, entanglement, and non-markovianity. *Phys. Rev. A* **95**, 042104 (2017).
62. He, Z., Zeng, H.-S., Li, Y., Wang, Q. & Yao, C. Non-markovianity measure based on the relative entropy of coherence in an extended space. *Phys. Rev. A* **96**, 022106 (2017).
63. Radhakrishnan, C., Chen, P.-W., Jambulingam, S., Byrnes, T. & Ali, Md. M. Time dynamics of quantum coherence and monogamy in a non-markovian environment. *Sci. Rep* **9**, 2363 (2019).
64. Chanda, T. & Bhattacharya, S. Delineating incoherent non-markovian dynamics using quantum coherence. *Ann. Phys.* **366**, 1 (2016).
65. Du, K.-D. et al. Detecting non-markovianity via quantified coherence: theory and experiments. *npj Quantum Inf.* **6**, 55 (2020).
66. Baumgratz, T., Cramer, M. & Plenio, M. B. Quantifying coherence. *Phys. Rev. Lett.* **113**, 140401 (2014).
67. Streltsov, A., Adesso, G. & Plenio, M. B. Colloquium: quantum coherence as a resource. *Rev. Mod. Phys.* **89**, 041003 (2017).
68. Yu, M. et al. Quantum fisher information measurement and verification of the quantum cramér-rao bound in a solid-state qubit. *NPJ Quantum Inf.* **8**, 56 (2022).
69. Zhang, X., Lu, X.-M., Liu, J., Ding, W. & Wang, X. Direct measurement of quantum fisher information. *Phys. Rev. A* **107**, 012414 (2023).
70. Luo, S. Quantum uncertainty of mixed states based on skew information. *Phys. Rev. A* **73**, 022324 (2006).
71. Tóth, G. & Petz, D. Extremal properties of the variance and the quantum fisher information. *Phys. Rev. A* **87**, 032324 (2013).
72. Iwakura, A., Matsuzaki, Y. & Kondo, Y. Engineered noisy environment for studying decoherence. *Phys. Rev. A* **96**, 032303 (2017).
73. Ho, L. B., Matsuzaki, Y., Matsuzaki, M. & Kondo, Y. Realization of controllable open system with NMR. *New J. Phys.* **21**, 093008 (2019).
74. Zhou, Z. et al. A new decoupling method for accurate quantification of polyethylene copolymer composition and triad sequence distribution with ^{13}C NMR. *J. Magn. Reson.* **187**, 225 (2007).

Acknowledgements

This work was supported by the Brazilian ministries MEC and MCTIC, and the Brazilian funding agencies CNPq (Grant No. 304891/2022-3), FAPESP (Grant No. 2017/03727-0), Coordenação de Aperfeiçoamento de Pessoal de Nível Superior–Brasil (CAPES) (Finance Code 001), and the Brazilian National Institute of Science and Technology of Quantum Information (INCT-IQ). D. P. P. also acknowledges Fundação de Amparo à Pesquisa e ao Desenvolvimento Científico e Tecnológico do Maranhão (FAPEMA).

Author contributions

D.O.S.P., F.B., and J.G.F. devised the scenario for concretely analyzing crossovers between QSLs. E.R.A. and J.G.F. performed the measurements. D.P.P. performed the QSL analytical and numerical analysis. F.B. determined the analytical solution for the open system dynamics. All authors analyzed and discussed the results and participated in the writing of the article.

Competing interests

The authors declare no competing interests.

Additional information

Supplementary information The online version contains supplementary material available at https://doi.org/10.1038/s42005-024-01634-5.

Correspondence and requests for materials should be addressed to Frederico Brito.

Peer review information *Communications Physics* thanks the anonymous reviewers for their contribution to the peer review of this work. A peer review file is available.